

In Situ STEM-EELS Observation of Nanoscale Interfacial Phenomena in All-Solid-State Batteries

Ziyang Wang,[†] Dhamodaran Santhanagopalan,^{†,‡} Wei Zhang,[§] Feng Wang,[§] Huolin L. Xin,[§] Kai He,[§] Juchuan Li,^{||} Nancy Dudney,^{||} and Ying Shirley Meng^{*,†}

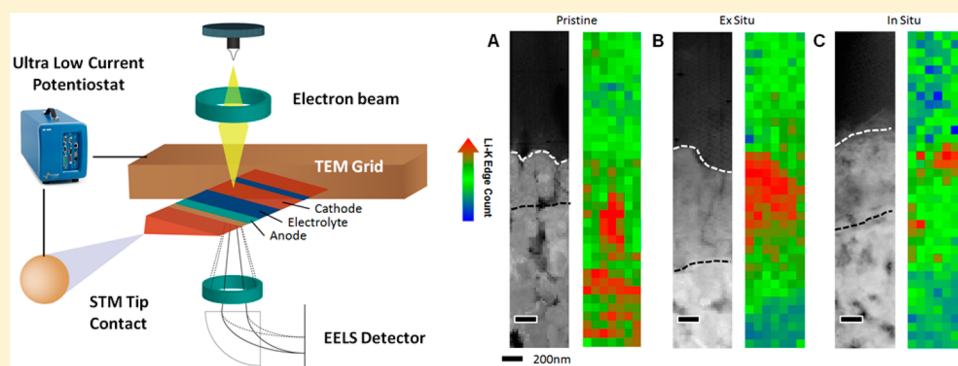
[†]Department of NanoEngineering, University of California, San Diego, La Jolla, California 92093, United States

[‡]Amrita Centre for Nanosciences and Molecular Medicine, Amrita Vishwa Vidyapeetham University, Kochi, Kerala 682041, India

[§]Brookhaven National Laboratory, Upton, New York 11973, United States

^{||}Material Science and Technology Division, Oak Ridge National Laboratory, Oak Ridge, Tennessee 37831, United States

Supporting Information



ABSTRACT: Behaviors of functional interfaces are crucial factors in the performance and safety of energy storage and conversion devices. Indeed, solid electrode–solid electrolyte interfacial impedance is now considered the main limiting factor in all-solid-state batteries rather than low ionic conductivity of the solid electrolyte. Here, we present a new approach to conducting in situ scanning transmission electron microscopy (STEM) coupled with electron energy loss spectroscopy (EELS) in order to uncover the unique interfacial phenomena related to lithium ion transport and its corresponding charge transfer. Our approach allowed quantitative spectroscopic characterization of a galvanostatically biased electrochemical system under in situ conditions. Using a $\text{LiCoO}_2/\text{LiPON}/\text{Si}$ thin film battery, an unexpected structurally disordered interfacial layer between LiCoO_2 cathode and LiPON electrolyte was discovered to be inherent to this interface without cycling. During in situ charging, spectroscopic characterization revealed that this interfacial layer evolved to form highly oxidized Co ions species along with lithium oxide and lithium peroxide species. These findings suggest that the mechanism of interfacial impedance at the $\text{LiCoO}_2/\text{LiPON}$ interface is caused by chemical changes rather than space charge effects. Insights gained from this technique will shed light on important challenges of interfaces in all-solid-state energy storage and conversion systems and facilitate improved engineering of devices operated far from equilibrium.

KEYWORDS: Lithium ion battery, thin film battery, in situ TEM, interfacial phenomena, solid electrolyte

All-solid-state lithium ion batteries have the potential to become the next generation of energy storage devices through the promise of higher energy density and better safety.¹ The use of solid state electrolyte enables the use of lightweight metallic lithium as the anode while substituting the commonly used flammable organic electrolyte. While the ionic conductivity of certain solid state electrolytes has converged on and in some cases surpassed organic liquid electrolytes,^{2–5} their widespread application has been limited by the large interfacial resistance between the solid electrolyte and electrode.^{1,6–8} In the case of amorphous lithium phosphorus oxynitride (LiPON) as the solid electrolyte, many studies have focused on methods to reduce the interfacial resistance through post deposition heat

treatment and off-axis deposition.^{9,10} However, the physical mechanism for the high lithium ion transfer impedance is still unclear. Space charge effects were thought to be the cause of interfacial resistance between high voltage spinel and LiPON,¹¹ while computational studies have indicated thermodynamic instability at various solid electrolyte–electrode interfaces.^{12,13} To truly understand the chemical reactions and phase transformations that occur at the electrode–electrolyte interface, dynamic analytical characterization of interfacial behavior far from equilibrium, that is, without relaxation and air

Received: March 15, 2016

Published: May 3, 2016

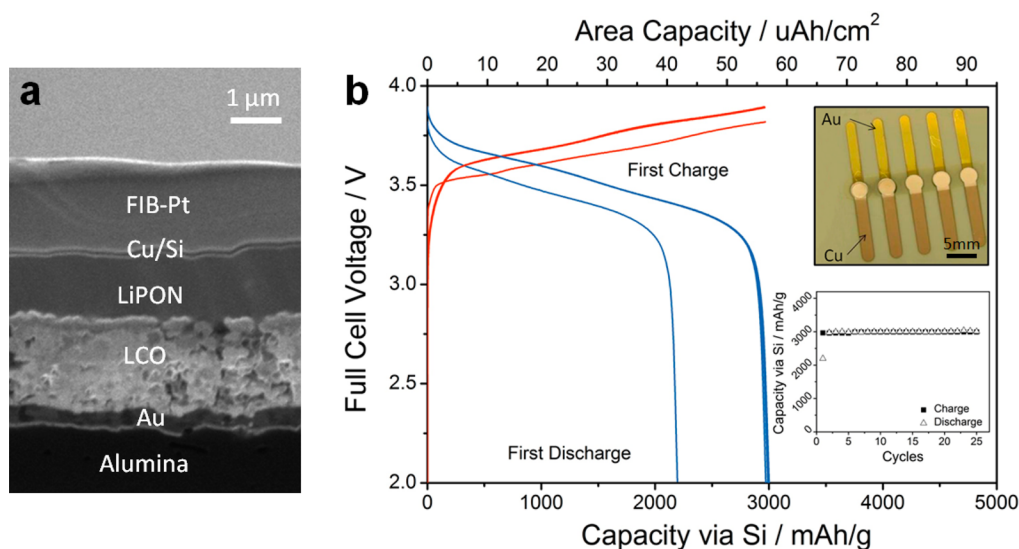


Figure 1. RF-magnetron sputtered all-solid-state batteries. (a) Cross sectional ion-beam image of the solid-state battery shows all the solid-state components. (b) The cycling profile of the solid-state batteries where the red lines denote charge profiles and the blue lines denote discharge profiles. The insets show the optical image of the solid-state batteries and the capacity versus cycle over 25 cycles.

exposure, is required and would be invaluable in designing advanced functional systems with low interfacial impedance.

Indeed, *ex situ* analytical characterization of solid–solid interface was first explored by Brazier et al. where a focused ion beam processed cross section of a cycled thin film battery was characterized in the TEM.¹⁴ Such preparation of a nanobattery offered an unprecedented high-resolution characterization of the solid electrolyte–electrode interface. However, the lack of electrochemical activity in the nanobatteries fabricated through their approach meant that dynamic changes could not be characterized under *in situ* conditions. Since then, *in situ* transmission electron microscopy has made great strides via other approaches involving the use of ionic liquids and liquid cells to observe morphological changes in lithium ion battery materials. Despite the advances, these approaches have not succeeded in the simultaneous application of three important experimental conditions: quantitative chemical characterization, galvanostatic current control, and *in situ* environment. *In situ* TEM studies exploring lithiation of anode nanowires lack electrochemical current control that prohibits quantitative interpretation of the observed structural, morphological, and chemical changes with respect to redox potentials, and more importantly, state of charge.^{15–22} Quantitative analytical characterization is inherently difficult in liquid cells as spatial resolution is diminished by the presence of a silicon nitride membrane and core-loss signal in electron energy loss spectroscopy (EELS) is overwhelmed by multiple scattering from the liquid electrolyte.^{23–25} Using electron holography, Yamamoto et al. observed the electric potential distribution at the LiCoO₂–Ohara solid electrolyte interface under *in situ* conditions.²⁶ However, the electrochemical cell was biased using cyclic voltammetry that did not offer state of charge control and substantial quantitative analysis of interfacial phenomena was not provided. Therefore, a new methodology is needed to provide *in situ* structural and quantitative chemical probing of interfacial phenomena in all-solid-state batteries.

Here, we demonstrate a new approach to *in situ* scanning transmission electron microscopy (STEM) coupled with electron energy loss spectroscopy (EELS) characterization of interfacial phenomena using solid state batteries with

simultaneous galvanostatic biasing. Our novel approach utilizes a carefully designed and controlled focused ion beam (FIB) fabrication procedure that enables electrochemically active nanobatteries to be galvanostatically biased in the FIB or TEM column.²⁷ With *in situ* biasing, we can avoid reactions due to air exposure and allow characterization of electrochemical systems without relaxation. Additionally, quantitative characterization of all-solid-state electrochemical systems is not hindered by the cell membranes or liquid electrolytes present in liquid cells. We have previously shown lithium plating at the anode/current collector interface along with interdiffusion of elements at the anode/electrolyte interface by using *ex situ* STEM-EELS analysis.²⁷ In this study, we report successful *in situ* STEM-EELS characterization of the cathode/electrolyte interface by galvanostatically biasing a solid state nanobattery. We discovered a disordered interface layer derived from layered LiCoO₂ inherent to the LiCoO₂/LiPON interface, suggesting that chemical instability leading to the formation of an ionic resistive layer is the main mechanism of interfacial impedance.

We deposited solid-state batteries consisting of 2 μm LiCoO₂ (cathode theoretical capacity of 140 μAh/cm² up to Li_{0.5}CoO₂), 80 nm amorphous Si (anode theoretical capacity of 66.7 μAh/cm² assuming Li_{3.75}Si), and 1.5 μm lithium phosphorus oxynitride LiPON electrolyte with Au and Cu as cathode and anode current collectors. The cathode and electrolyte were deposited by RF-magnetron sputtering, while Au, Cu, and Si were deposited by DC sputtering. Cross sectional ion-beam image of the solid-state battery is shown in Figure 1A. In order to measure the bulk performance of the as-deposited solid-state batteries, we cycled a cell at C/10 for five cycles and C/2 for an additional 20 cycles while limiting full cell capacity to 3000 mAh/g relative to the silicon anode. Detailed fabrication procedure and cycling parameters are described in Supporting Information. There is an initial irreversible capacity loss on the first cycle with Coulombic efficiency of 75% as shown in Figure 1B, while subsequent cycles had Coulombic efficiencies of nearly 100%. Because the cathode has almost twice the capacity of the anode, the cathode is able to provide more charge/discharge capacity on the second cycle. Once we have established proper bulk electrochemistry of the all-solid-state

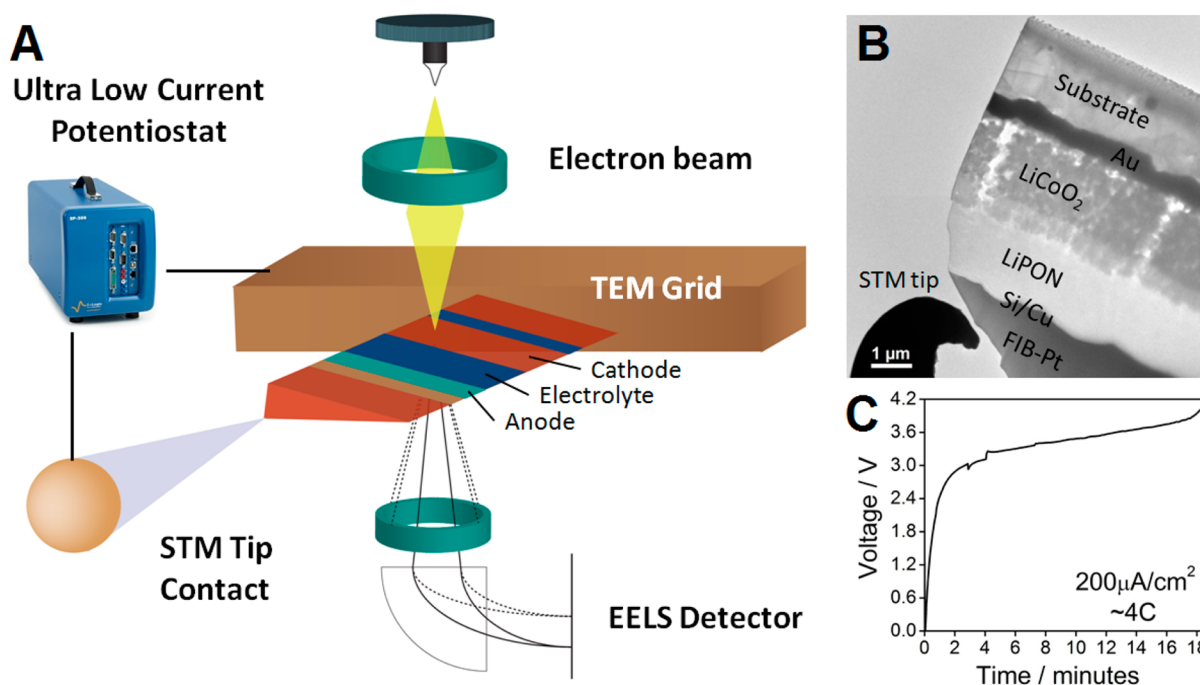


Figure 2. Schematic of in situ TEM biasing of nanobattery. (A) Schematic of the experimental setup of nanobattery mounted on a TEM grid shows the triangular geometry of the cell. The cathode is electrically connected to the grid and a piezo-controlled STM tip makes contact with the anode current collector. (B) TEM bright field image of STM tip connecting a nanobattery. (C) Electrochemical profile of the in situ cell galvanostatically charged in the TEM.

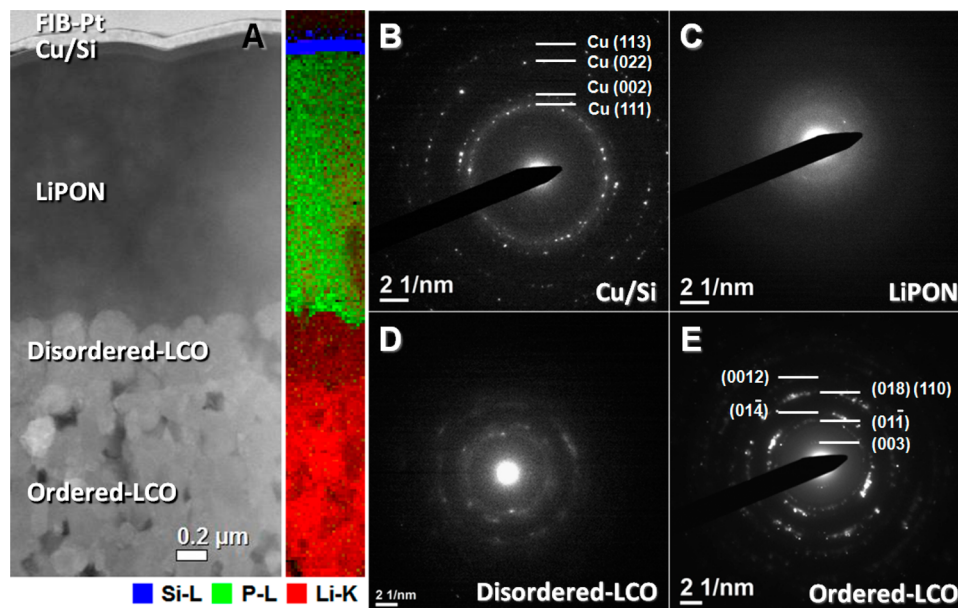


Figure 3. Scanning transmission electron microscope imaging of solid-state battery. (A) HAADF image of the nanobattery stack along with elemental mapping of Li (red), P (green), and Si (blue). (B–E) SAED obtained from (B) Cu/Si, (C) LiPON, (D) disordered LCO layer, and (E) ordered LCO layer.

thin film battery, we used other samples fabricated using the same procedure for in situ TEM experiments. The first cycle irreversibility in contrast with subsequent high Coulombic efficiencies is the focus of STEM-EELS studies conducted.

In order to perform in situ experiments, we devised a set of FIB fabrication conditions that will retain electrochemical activity in a nanobattery that can be charged galvanostatically in the FIB chamber or transferred to a TEM column for in situ galvanostatic biasing. A set of optimized beam current and pixel

dwell time conditions was required to minimize ion damage and preserve electrochemical activity. The process of ion beam optimization and effects of pixel dwell time are detailed in our previous publications,^{27,28} while details of the fabrication conditions and procedures are presented in [Supporting Information](#) and [Supporting Video 1](#). There are three samples that were characterized in this study: pristine, ex situ, and in situ. The pristine sample was prepared using the optimized procedures and thinned to ~ 80 nm in the FIB without

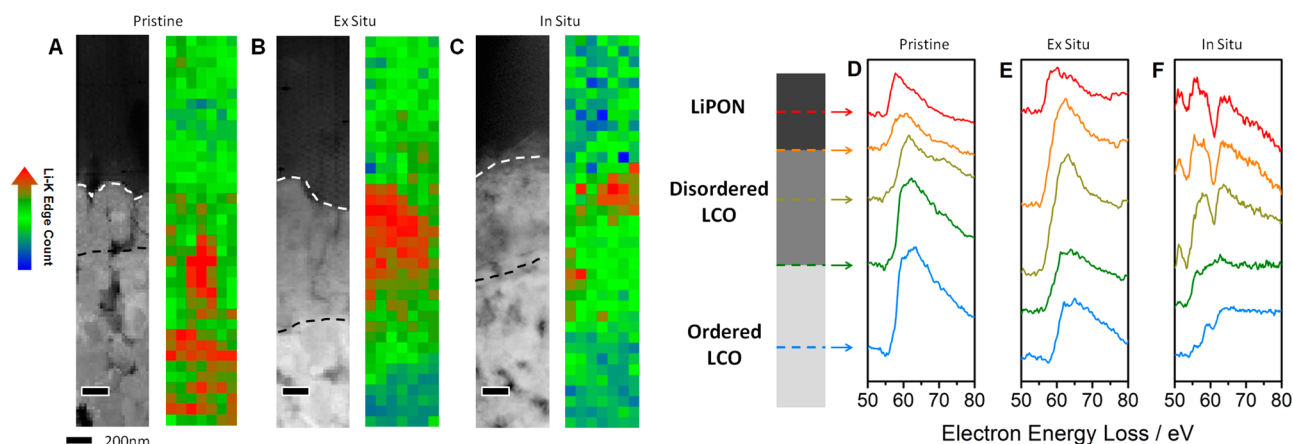


Figure 4. STEM image and EELS characterization. (A–C) HAADF image of the nanobattery stack along with Li K-edge concentration mapping of (A) pristine, (B) ex situ, and (C) in situ samples with scale bar represents 200 nm. (D–F) Li K-edge spectra from various parts of the layers are displayed for (D) pristine, (E) ex situ, and (F) in situ samples.

electrochemical biasing. The ex situ sample was made from a $2 \mu\text{m} \times 10 \mu\text{m}$ rectangular nanobattery charged to 4.2 V in the FIB chamber and subsequently thinned down to ~ 80 nm for TEM. The in situ sample was made from a $1 \mu\text{m} \times 10 \mu\text{m}$ triangular nanobattery that was transferred to the TEM and charged to 4.2 V with the e-beam off to avoid accumulation of beam damage on LiPON. Schematic of the experimental setup is shown in Figure 2A. The tip of the triangular geometry is thin enough (~ 80 nm) for EELS characterization (Figure 2B) and the electrochemical profile is shown in Figure 2C. An additional video of a separate nanobattery charged in the TEM with the beam on is shown in Supporting Video 2 with electrochemical profile shown in Supporting Information Figure S1. As the LiPON electrolyte is highly sensitive to electron beam dosage, we have determined the optimal electron dosage to avoid significant beam damage for low loss EELS data collection in our previous publications.^{27,28} Details of STEM-EELS electron beam and collection conditions are provided in Supporting Information. STEM-EELS analysis comparing the morphology, structure, lithium concentration profile, and chemical bonding of different layers in these three samples will be presented and discussed.

High-angle annular dark-field (HAADF) images of the pristine sample displayed distinct layers of the expected solid-state components (Figure 3A). We also conducted elemental mapping by low loss EELS to show the expected distribution of Li, P, and Si in their respective components. Selected area electron diffraction showed amorphous silicon with the copper current collector (Figure 3B) and amorphous LiPON electrolyte (Figure 3C) as expected. We observed, however, an unexpected and previously unreported interfacial layer, 250–300 nm thick, between LiCoO_2 (cathode) and LiPON (electrolyte) in all samples. This disordered interface layer is derived from LCO and hence it will be referred to as the disordered LCO layer while the rest of the LCO layer will be referred to as the ordered LCO layer. The disordered LCO layer showed diffuse rings in selected area electron diffraction that do not index to layered lithium cobalt oxide structure with $R\bar{3}m$ symmetry (Figure 3D), while the ordered LCO layer showed distinct spots for a polycrystalline layered LCO (Figure 3E). From the integrated radial intensity of the electron diffraction pattern (Supporting Information Figure S2), we can reasonably speculate that the interfacial layer is composed of a

highly disordered solid-solution of Li_2O and CoO in rocksalt structure decomposed from layered LCO. The broadness of the rocksalt peaks indicates that there is variation in the lattice parameter of the disordered phase. This could be caused by nonuniform local lithium to transition metal ratio leading to local lithium excess and local lithium deficiency domains. Despite the disordered nature of the interfacial layer, lithium conduction is still possible in percolating channels that could arise in regions with lithium excess stoichiometry as proposed by Lee et al.²⁹

Having discovered a distinct interfacial layer between the cathode and electrolyte layers, we conducted low loss EELS mapping of the interfacial region to explore the ionic transport of lithium. Given the convoluted nature of Li K-edge with Co M-edge and the shifting of Li K-edge based on chemical environment, an integration window of 5 eV spanning from 55 to 60 eV was chosen. It is important to note that intensity contributions in this integration window can only arise from metallic lithium or lithium containing compounds such as lithium carbonate, lithium oxide,³⁰ or LiPON with small potential contributions from CoO rocksalt. This is because LiCoO_2 standards resulted in slight negative intensity due to Fano Resonance³¹ and Co_3O_4 standards showed minimal intensity in the energy range (Supporting Information Figure S3A). Compared to the pristine sample (Figure 4A), the ex situ (Figure 4B) sample has significant integrated intensity in the disordered LCO layer contouring to the physical morphology of the LiPON/disordered LCO interface. This confirms our previous study where ex situ lithium accumulation was observed at the LCO/LiPON interface.²⁷ Integrated intensity mapping of the in situ sample (Figure 4C) also showed increased counts in the disordered layer indicating lithium accumulation occurs during charging. Figure 4D–F shows selected spectra taken from LiPON, disordered LCO layer, ordered LCO layer, and their interfaces from the three samples. For the in situ sample, Li K-edge intensity is fairly low in LiPON due to in situ charged LiPON that is more sensitive to beam effects. After electrochemical charging, small changes in the solid state electrolyte can cause this particular region of the sample to be more susceptible to e-beam induced charging and heating since the electrolyte is inherently more insulating than the electrodes. This can result in beam damage even in the optimized beam conditions. These findings must be taken into

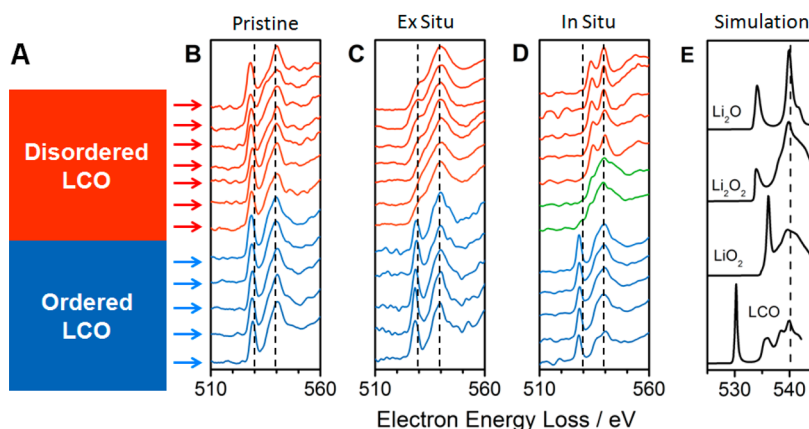


Figure 5. O K-edge Electron Energy Loss Spectra. (A) Schematic of the spatial location of each line scan. (B–D) O K-edge from the disordered LCO layer (red) and ordered LCO layer (blue) are shown for (B) pristine sample, (C) ex situ sample, and (D) in situ sample. The green spectra show O K-edge from the disordered LCO/ordered LCO interface. (E) FEFF9 EELS simulation of LiCoO_2 , Li_2O , Li_2O_2 , LiO_2 O K-edge.

consideration along with more quantitative high loss EELS analysis to complement the interpretation.

Indeed, high loss EELS conducted on LCO layers revealed chemical changes in Co–O bonding structure during lithium ion transport. By simultaneously probing O K-edge and Co L-edge, we can observe changes in chemical bonding between oxygen 2p orbitals and cobalt 3d orbitals.³² Through theoretical calculations and experimental results, it has been demonstrated that O K-pre-edge is a strong indicator of hybridized bonding between transition metal atom and oxygen atom.^{33–35} Conversely, disappearance of O K-pre-edge is normally accompanied by formation of oxygen vacancies, structural changes such as transition metal migration, and reduction of transition metal resulting in ionic bonding that occurs in rocksalt structures.^{36–39} Additionally, analysis of the ratio between Co L_3 and L_2 white lines is complementary to changes in O K-edge as the hybridization of oxygen 2p and cobalt 3d is highly affected by the oxidation state of the cobalt ion. The raw spectra of Co L-edge of three samples are shown in Supporting Information Figure S4. Using standards of LCO, Co_3O_4 , and CoO, the L_3/L_2 ratios were calculated for Co^{3+} , $\text{Co}^{2.66+}$, and Co^{2+} respectively (Supporting Information Figure S3C). Upon analyzing these high loss EELS features of the three samples, we can begin to understand the chemical changes that occur in situ and ex situ.

We analyzed the high loss edges at various positions of the LCO layers (Figure 5A) in the three samples to observe changes in the chemical bonding of oxygen with cobalt. In the pristine sample (Figure 5B), O K-pre-edge (~ 530 eV) is present in the disordered LCO layer as well as the ordered LCO layer even though the interfacial layer is highly disordered. This implies that the local cobalt and oxygen bonding in the pristine disordered LCO layer is still similar to the hybridization of cobalt 3d and oxygen 2p orbitals observed in typical layered lithium cobalt oxide. Co L_3/L_2 ratio (Figure 6 red line) expectedly remains fairly stable around ~ 2.15 which corresponds to mostly Co^{3+} throughout both the LCO layers.⁴⁰ In the ex situ sample (Figure 5C), oxygen evolution after relaxation and air exposure during transfer from FIB to TEM cause O K-pre-edge to decrease significantly in the disordered LCO layer. After enough relaxation time, the combination of CoO rocksalt formation as observed by SAED of the disordered LCO layer in ex situ charged nanobattery (Supporting Information Figure S5) along with oxygen evolution reaction

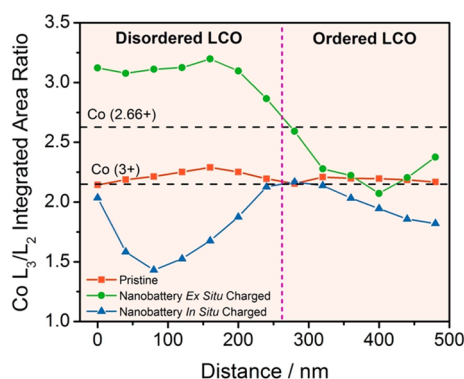


Figure 6. Co L_3/L_2 ratio analysis of electron energy loss spectra. The Co L_3/L_2 ratios calculated by a two-step method in the ratio of 2:1 to account for level degeneracy are shown. As cobalt becomes more oxidized, the ratio shifts to a lower value and vice versa. The dotted line denotes the separation between the disordered LCO layer and the ordered LCO layer.

resulted in a more ionic bond between Co 3d orbital and O 2p orbital leading to a decrease of O K-pre-edge intensity. This chemical change can also be confirmed by the increase of Co L_3/L_2 ratio (Figure 6 green line) to over 3.0 in the disordered layer, consistent with reduced cobalt in CoO rocksalt.

More importantly, chemical changes that occur in the disordered layer that can be missed if the characterization is done ex situ. O K-pre-edge shifts to a higher energy loss in the disordered LCO layer of the in situ sample (Figure 5D). During in situ charging, accumulated lithium ions react with oxygen to form phase separated Li_2O or Li_2O_2 . From EELS simulations using FEFF9 of O K-edge⁴¹ based on lithium oxide and lithium peroxide (Figure 5E), we can see that O K-pre-edge shifts to a higher energy level of ~ 535 eV, which is consistent with in situ observations. It is important to note that in bulk, artifact-free soft X-ray absorption spectroscopy of lithium oxide, the O K-pre-edge shift is also confirmed.⁴² Thus, the shift of O K-pre-edge in the in situ sample is indeed caused by formation of lithium oxides and not a result of beam artifacts. At the same time, the local CoO_6 octahedron in the pristine disordered LCO is destroyed during charging with buildup of lithium oxides. Lithium oxide species formed during the in situ charge will react with CO_2 and H_2O present in the air to form neutral oxygen molecules, Li_2CO_3 , and LiOH which further reacts to

form Li_2CO_3 . These factors result in the decrease of O K-pre-edge in the ex situ interfacial layer. It is interesting to note that at the interface between the disordered LCO layer and the ordered LCO layer of the in situ sample (green spectra in Figure 5D), O K-pre-edge has decreased in intensity. It is possible that oxygen evolution reaction and CoO formation start at this interface and propagate through the disordered LCO layer.

We also observed Co L_3/L_2 ratio of the in situ sample (Figure 6 blue line) decreases to ~ 1.75 in the ordered LCO layer indicating slight oxidation of cobalt. On the other hand, the disordered LCO layer showed highly oxidized cobalt as indicated by a L_3/L_2 ratio of ~ 1.5 at the center of the disordered layer. There has not been enough relaxation time for oxygen evolution reaction to occur in order to charge balance. At the interface of disordered and ordered LCO layer of the in situ sample, we see that L_3/L_2 ratio increases again to ~ 2.25 confirming that oxygen evolution and CoO formation reactions begin at this interface as observed by O K-edge. Given enough relaxation time, oxygen evolution acts as electron donors that reduce oxidized cobalt atoms as rocksalt cobalt oxide forms. Although references of Co L_3/L_2 ratio for highly oxidized cobalt have been elusive due to the unstable nature of tetravalent cobalt,⁴³ we can take advantage of galvanostatic charge to estimate the average cobalt oxidation state. From Figure 2C, we estimate a total charge of $60 \mu\text{Ah}/\text{cm}^2$ was needed to charge the cell to 4.2 V. While this is far from the full capacity of the cathode, it is close to the full capacity of the silicon anode. Nonetheless, we can estimate an overall extraction of 0.21 Li ions per unit of LCO and a cobalt oxidation state of +3.21. With galvanostatic charging, we are able to correlate spectroscopic observations with the lithium content of the electrochemical system. A second in situ STEM-EELS experiment was also conducted and analysis of the data is shown in Supporting Information figure S6.

As seen from the STEM-EELS characterization, the disordered LCO layer is present in the pristine sample and behaves very differently from the ordered LCO layer. First, the disordered layer is not caused by damages from FIB processing; as selected area electron diffraction on a FIB processed LCO thin film sample without LiPON showed crystalline structure at the surface of the film (Supporting Information Figure S7). Additionally, energy of the sputtered atoms in RF sputtering in the range of tens of electronvolts, is much less than 30 kV used in FIB.^{44,45} Hence, it is unlikely that the disordered layer formed as a result of the sputter deposition process of LiPON on LCO. We speculate that such a disordered structure could form as a result of an intrinsic chemical reaction between deposited LCO and LiPON causing structural changes.¹² Similarly, LiPON deposition on LiMn_2O_4 thin films have been shown to initially delithiate the spinel material.⁴⁶ This observation implies that it is important for the cathode material to be chemically and electrochemically stable when paired with LiPON electrolyte.

Presence of the disordered layer can have major effects on the performance of the battery. The dQ/dV analysis of full cell voltage profile clearly reveals the existence of two redox peaks at 3.55 and 3.60 V on the first charge that do not provide reversible discharge capacity and do not appear on subsequent cycles (Supporting Information Figure S8). A significant portion of this first cycle full cell irreversible capacity of solid-state batteries could be due to lithium accumulation and chemical changes in the interfacial layer, as well as first cycle

irreversibility of the silicon anode. It has been shown that silicon thin films of <100 nm thickness has $\sim 20\%$ first cycle irreversibility.^{47–49} Surprisingly this disordered layer has rather good lithium ion transport, though the atomistic details of this layer are still lacking. Using additional commercially RF sputtered LCO/LiPON/Li cells, we further observed that the disordered layer grows significantly thicker when cycled at 80°C as compared to those cycled at 25°C . The growth of this disordered interfacial layer is accompanied by rapid decay in reversible capacity after 250 cycles. Analysis of impedance spectroscopy taken every 50 cycle at the charged state showed continuously increasing interfacial resistances of the cells. These detailed findings are under revision elsewhere.⁵⁰

Finally, differences between in situ and ex situ observations of O K-edge and Co L-edge highlight the importance of dynamic in situ characterization. In situ characterization monitors electronic structure changes in interfaces without prolonged time relaxation, air exposure, and other factors that could interfere with sample properties. The combination of electron diffraction, STEM imaging, and analytical EELS characterization has given critical insight into the impact of interfacial phenomena in first cycle irreversible capacity loss of solid-state batteries. With recent improvements in electron microscope and direct detectors, greater energy resolution (<0.1 eV) and higher temporal resolution (submillisecond) can be achieved. Analytical information gathered through this novel technique will help scientists in the field of all-solid-state battery to establish new design rules for solid–solid interfaces and improve electrochemical performance and lifetime of such systems.

In conclusion, STEM-EELS characterization of solid-state batteries revealed a disordered interfacial layer between cathode and electrolyte that accumulates lithium and evolves to rocksalt CoO after cycling. This layer could form as a result of depositing cathode materials that are structurally unstable in highly delithiated states on LiPON. With in situ STEM-EELS characterization of solid–solid interfaces enabled through our unique procedure, we observed $\text{Li}_2\text{O}/\text{Li}_2\text{O}_2$ formation as an intermediate compound of oxygen evolution reaction as the disordered interfacial layer eventually formed a rocksalt structure ex situ. Increasing thickness of this layer would lead to rapid capacity decay as more of the cathode will be rendered electrochemically inactive. Because oxygen evolution reaction at high voltage is common in several oxide-based cathode materials, it is critical to solve interfacial issues for better safety and long-term cycling. Our novel methodology developed to study dynamics at the nanoscale could be applied to various solid-state devices beyond solid-state batteries, such as solid-state solar cells, metal air fuel cells, and field effect transistors.

■ ASSOCIATED CONTENT

Supporting Information

The Supporting Information is available free of charge on the ACS Publications website at DOI: [10.1021/acs.nanolett.6b01119](https://doi.org/10.1021/acs.nanolett.6b01119).

Experimental details for thin film battery fabrication, nanobattery fabrication by focused ion beam, STEM-EELS collection and analysis. (PDF)

Video of thin film liftout procedure using focused ion beam. (AVI)

Video of a separate nanobattery charged in the TEM with the beam on. (AVI)

AUTHOR INFORMATION

Corresponding Author

*E-mail: shmeng@ucsd.edu.

Author Contributions

Z.W., D.S., and Y.S.M. designed the experimental plan. Z.W. and D.S. conducted the in situ and ex situ experiments with FIB and analyzed the STEM-EELS data. H.L.X., K.H., W.Z., and F.W. carried out the STEM-EELS measurements. J.L. and N.D. prepared the solid-state battery samples. Z.W., D.S., and Y.S.M. prepared the manuscript, which incorporates critical inputs from all authors.

Notes

The authors declare no competing financial interest.

ACKNOWLEDGMENTS

UCSD acknowledges the funding support for the development of all-solid-state battery and in situ FIB and TEM holder design by the U.S. Department of Energy, Office of Basic Energy Sciences, under award number DE-SC0002357. The collaboration with national laboratories is made possible with partial support of the Northeastern Center for Chemical Energy Storage, an Energy Frontier Research Center funded by the U.S. Department of Energy, Office of Basic Energy Sciences, under award number DE-SC0001294. TEM studies and part of FIB work were carried out at Center for Functional Nanomaterials, which is a U.S. DOE Office of Science Facility, at Brookhaven National Laboratory under Contract No. DE-SC0012704. Thin film batteries were fabricated at Oak Ridge National Laboratory with support of the U.S. Department of Energy, Office of Science, Basic Energy Sciences (BES), Materials Sciences and Engineering Division. W.Z. was supported by the Laboratory Directed Research and Development (LDRD) program at Brookhaven National Laboratory, under the ward No. 13-022. D.S. is thankful to SERB, India for Ramanujan Fellowship.

REFERENCES

- Luntz, A. C.; Voss, J.; Reuter, K. J. *Phys. Chem. Lett.* **2015**, *6* (22), 4599–4604.
- Kamaya, N.; Homma, K.; Yamakawa, Y.; Hirayama, M.; Kanno, R.; Yonemura, M.; Kamiyama, T.; Kato, Y.; Hama, S.; Kawamoto, K.; Mitsui, A. *Nat. Mater.* **2011**, *10* (9), 682–686.
- Inaguma, Y.; Liqun, C.; Itoh, M.; Nakamura, T.; Uchida, T.; Ikuta, H.; Wakihara, M. *Solid State Commun.* **1993**, *86* (10), 689–693.
- Kanno, R.; Murayama, M. *J. Electrochem. Soc.* **2001**, *148* (7), A742–A746.
- Murugan, R.; Thangadurai, V.; Weppner, W. *Angew. Chem., Int. Ed.* **2007**, *46* (41), 7778–7781.
- Kotobuki, M.; Munakata, H.; Kanamura, K.; Sato, Y.; Yoshida, T. *J. Electrochem. Soc.* **2010**, *157* (10), A1076–A1079.
- Sakuda, A.; Hayashi, A.; Tatsumisago, M. *Chem. Mater.* **2010**, *22* (3), 949–956.
- Ohta, N.; Takada, K.; Zhang, L.; Ma, R.; Osada, M.; Sasaki, T. *Adv. Mater.* **2006**, *18* (17), 2226–2229.
- Iriyama, Y.; Kako, T.; Yada, C.; Abe, T.; Ogumi, Z. *J. Power Sources* **2005**, *146* (1–2), 745–748.
- Iriyama, Y.; Kako, T.; Yada, C.; Abe, T.; Ogumi, Z. *Solid State Ionics* **2005**, *176* (31–34), 2371–2376.
- Yada, C.; Ohmori, A.; Ide, K.; Yamasaki, H.; Kato, T.; Saito, T.; Sagane, F.; Iriyama, Y. *Advanced Energy Materials* **2014**, *4*, (9), n/a-n/a.
- Richards, W. D.; Miara, L. J.; Wang, Y.; Kim, J. C.; Ceder, G. *Chem. Mater.* **2016**, *28* (1), 266–273.
- Miara, L. J.; Richards, W. D.; Wang, Y. E.; Ceder, G. *Chem. Mater.* **2015**, *27* (11), 4040–4047.
- Brazier, A.; Dupont, L.; Dantras-Laffont, L.; Kuwata, N.; Kawamura, J.; Tarascon, J. M. *Chem. Mater.* **2008**, *20* (6), 2352–2359.
- Liu, X. H.; Wang, J. W.; Huang, S.; Fan, F.; Huang, X.; Liu, Y.; Krylyuk, S.; Yoo, J.; Dayeh, S. A.; Davydov, A. V.; Mao, S. X.; Picraux, S. T.; Zhang, S.; Li, J.; Zhu, T.; Huang, J. Y. *Nat. Nanotechnol.* **2012**, *7* (11), 749–756.
- Liu, X. H.; Zheng, H.; Zhong, L.; Huang, S.; Karki, K.; Zhang, L. Q.; Liu, Y.; Kushima, A.; Liang, W. T.; Wang, J. W.; Cho, J. H.; Epstein, E.; Dayeh, S. A.; Picraux, S. T.; Zhu, T.; Li, J.; Sullivan, J. P.; Cumings, J.; Wang, C.; Mao, S. X.; Ye, Z. Z.; Zhang, S.; Huang, J. Y. *Nano Lett.* **2011**, *11*, 3312–3318.
- Liu, X. H.; Zhang, L. Q.; Zhong, L.; Liu, Y.; Zheng, H.; Wang, J. W.; Cho, J.-H.; Dayeh, S. A.; Picraux, S. T.; Sullivan, J. P.; Mao, S. X.; Ye, Z. Z.; Huang, J. Y. *Nano Lett.* **2011**, *11*, 2251–2258.
- Liu, X. H.; Huang, S.; Picraux, S. T.; Li, J.; Zhu, T.; Huang, J. Y. *Nano Lett.* **2011**, *11* (9), 3991–3997.
- Huang, J. Y.; Zhong, L.; Wang, C. M.; Sullivan, J. P.; Xu, W.; Zhang, L. Q.; Mao, S. X.; Hudak, N. S.; Liu, X. H.; Subramanian, A.; Fan, H.; Qi, L.; Kushima, A.; Li, J. *Science* **2010**, *330* (6010), 1515–1520.
- Wang, C. M.; Xu, W.; Liu, J.; Zhang, J. G.; Saraf, L. V.; Arey, B. W.; Choi, D.; Yang, Z. G.; Xiao, J.; Thevuthasan, S.; Baer, D. R. *Nano Lett.* **2011**, *11*, 1874–1880.
- Wang, F.; Yu, H.-C.; Chen, M.-H.; Wu, L.; Pereira, N.; Thornton, K.; Van der Ven, A.; Zhu, Y.; Amatucci, G. G.; Graetz, J. *Nat. Commun.* **2012**, *3*, 1201.
- Zhu, Y.; Wang, J. W.; Liu, Y.; Liu, X.; Kushima, A.; Liu, Y.; Xu, Y.; Mao, S. X.; Li, J.; Wang, C.; Huang, J. Y. *Adv. Mater.* **2013**, *25* (38), 5461–5466.
- Gu, M.; Parent, L. R.; Mehdi, B. L.; Unocic, R. R.; McDowell, M. T.; Sacci, R. L.; Xu, W.; Connell, J. G.; Xu, P.; Abellan, P.; Chen, X.; Zhang, Y.; Perea, D. E.; Evans, J. E.; Lahun, L. J.; Zhang, J.-G.; Liu, J.; Browning, N. D.; Cui, Y.; Arslan, I.; Wang, C.-M. *Nano Lett.* **2013**, *13* (12), 6106–6112.
- Mehdi, B. L.; Qian, J.; Nasybulin, E.; Park, C.; Welch, D. A.; Faller, R.; Mehta, H.; Henderson, W. A.; Xu, W.; Wang, C. M.; Evans, J. E.; Liu, J.; Zhang, J. G.; Mueller, K. T.; Browning, N. D. *Nano Lett.* **2015**, *15* (3), 2168–2173.
- Holtz, M. E.; Yu, Y.; Gunceler, D.; Gao, J.; Sundararaman, R.; Schwarz, K. A.; Arias, T. A.; Abruña, H. D.; Muller, D. A. *Nano Lett.* **2014**, *14* (3), 1453–1459.
- Yamamoto, K.; Iriyama, Y.; Asaka, T.; Hirayama, T.; Fujita, H.; Fisher, C. A. J.; Nonaka, K.; Sugita, Y.; Ogumi, Z. *Angew. Chem., Int. Ed.* **2010**, *49*, 4414–4417.
- Santhanagopalan, D.; Qian, D.; McGilvray, T.; Wang, Z.; Wang, F.; Camino, F.; Graetz, J.; Dudney, N.; Meng, Y. S. *J. Phys. Chem. Lett.* **2014**, *5* (2), 298–303.
- Ziying, W.; Ying Shirley, M. Analytical Electron Microscopy Study of All Solid-State Batteries. In *Handbook of Solid State Batteries*; World Scientific: New York, 2015; Vol. 6, pp 109–131.
- Lee, J.; Urban, A.; Li, X.; Su, D.; Hautier, G.; Ceder, G. *Science* **2014**, *343* (6170), 519–522.
- Wang, F.; Graetz, J.; Moreno, M. S.; Ma, C.; Wu, L.; Volkov, V.; Zhu, Y. *ACS Nano* **2011**, *5* (2), 1190–1197.
- Fano, U. *Phys. Rev.* **1961**, *124* (6), 1866–1878.
- Graetz, J.; Hightower, A.; Ahn, C. C.; Yazami, R.; Rez, P.; Fultz, B. *J. Phys. Chem. B* **2002**, *106* (6), 1286–1289.
- Stemmer, S.; Sane, A.; Browning, N. D.; Mazanec, T. J. *Solid State Ionics* **2000**, *130* (1–2), 71–80.
- Aydinol, M. K.; Kohan, A. F.; Ceder, G.; Cho, K.; Joannopoulos, J. *Phys. Rev. B: Condens. Matter Mater. Phys.* **1997**, *56* (3), 1354–1365.
- Ceder, G.; Ven, A. V. d.; Marianetti, C.; Morgan, D. *Modell. Simul. Mater. Sci. Eng.* **2000**, *8* (3), 311–321.
- Carroll, K. J.; Qian, D.; Fell, C.; Calvin, S.; Veith, G. M.; Chi, M.; Baggetto, L.; Meng, Y. S. *Phys. Chem. Chem. Phys.* **2013**, *15* (26), 11128–11138.
- Xu, B.; Fell, C. R.; Chi, M.; Meng, Y. S. *Energy Environ. Sci.* **2011**, *4* (6), 2223–2233.

- (38) Fell, C. R.; Qian, D.; Carroll, K. J.; Chi, M.; Jones, J. L.; Meng, Y. S. *Chem. Mater.* **2013**, *25* (9), 1621–1629.
- (39) Hwang, S.; Chang, W.; Kim, S. M.; Su, D.; Kim, D. H.; Lee, J. Y.; Chung, K. Y.; Stach, E. A. *Chem. Mater.* **2014**, *26* (2), 1084–1092.
- (40) Graetz, J. *Electronic Environments and Electrochemical Properties of Lithium Storage Materials*; California Institute of Technology: Pasadena, CA, 2003.
- (41) Moreno, M. S.; Jorissen, K.; Rehr, J. J. *Micron* **2007**, *38* (1), 1–11.
- (42) Qiao, R.; Chuang, Y.-D.; Yan, S.; Yang, W. *PLoS One* **2012**, *7* (11), e49182.
- (43) Amatucci, G. G.; Tarascon, J. M.; Klein, L. C. *J. Electrochem. Soc.* **1996**, *143* (3), 1114–1123.
- (44) Kusano, E.; Kobayashi, T.; Kashiwagi, N.; Saitoh, T.; Saiki, S.; Nanto, H.; Kinbara, A. *Vacuum* **1999**, *53* (1–2), 21–24.
- (45) Kadlec, S.; Quaeqhaegens, C.; Knuyt, G.; Stals, L. M. *Surf. Coat. Technol.* **1997**, *89* (1–2), 177–184.
- (46) Iriyama, Y.; Nishimoto, K.; Yada, C.; Abe, T.; Ogumi, Z.; Kikuchi, K. *J. Electrochem. Soc.* **2006**, *153* (5), A821–A825.
- (47) Chan, C. K.; Peng, H.; Liu, G.; McIlwrath, K.; Zhang, X. F.; Huggins, R. A.; Cui, Y. *Nat. Nanotechnol.* **2008**, *3* (1), 31–35.
- (48) Kasavajula, U.; Wang, C.; Appleby, A. J. *J. Power Sources* **2007**, *163* (2), 1003–1039.
- (49) Li, J.; Dozier, A. K.; Li, Y.; Yang, F.; Cheng, Y.-T. *J. Electrochem. Soc.* **2011**, *158* (6), A689–A694.
- (50) Wang, Z.; Lee, J. Z.; Xin, H.; Han, L.; Grillon, N.; Guy-Bouyssou, D.; Bouyssou, E.; Proust, P.; Meng, Y. S. *J. Power Sources* **2016**, under revision.